



# Engineering Notes

## Postcapture Dynamics and Experimental Validation of Subtethered Space Debris

Kirk Hovell\* and Steve Ulrich<sup>†</sup>

Carleton University, Ottawa, Ontario K1S 5B6, Canada

DOI: 10.2514/1.G003049

### Nomenclature

$\mathbf{A}$	=	attitude matrix
$\mathbf{a}$	=	tether attachment point on the body with respect to its center of mass, m
$c$	=	tether damping coefficient, (N · s)/m
$\mathbf{F}$	=	force vector components, N
$\mathcal{F}_x$	=	reference frame $x$
$J_{zz}$	=	moment of inertia, kg · m <sup>2</sup>
$k(\Delta L)$	=	tether stiffness as a function of tether stretch, N/m
$L, \Delta L, L_0$	=	tether length vector components, stretch, and nominal length, m
$m$	=	mass, kg
$\mathbf{r}$	=	position vector components, m
$\theta$	=	angle, deg
$\boldsymbol{\omega}$	=	angular rate vector components, deg / s

### Subscripts

$i$	=	$i$ th subtether
$m$	=	main tether
$s$	=	single tether
$t, c, j$	=	target, chaser, and junction, respectively

### Superscripts

$T$	=	transpose
$\times$	=	skew-symmetric matrix

## I. Introduction

THE space debris population poses safety hazards to operational spacecraft and has exponential growth, as described by the Kessler syndrome [1]. Active debris removal is essential for the continued use of popular Earth orbits, and it often consists of launching a chaser spacecraft that performs a rendezvous with the target debris [2]. A connection is then made with the debris, which is used to stabilize the debris and then tow it into a lower orbit, where it is released to decay into the atmosphere. Flexible tethers are a popular method for establishing a connection between the chaser and the

target. Tethered space objects are referred to as a tethered spacecraft system (TSS).

There are three phases to the removal of debris using a TSS: 1) establishing the TSS, 2) detumbling/despinning the debris in preparation for towing, and 3) towing the stabilized debris out of orbit. A target is tumbling when it has angular rates about all three axes, and it is spinning when it has an angular rate about a single axis. This Note focuses on the despinning aspect of the debris removal mission.

Aslanov and Yudinsev established the equations regarding the attitude motion of the target during towing [3,4], which they then extended to include effects such as flexible appendages [5] and fuel sloshing [6]. Aslanov and Ledkov studied debris towing when considering atmospheric effects [7]. Preliminary towing experiments have been recently performed under various static initial conditions in an air-bearing facility [8]. However, discrepancies between the experimental and simulated results were reported. Other researchers have investigated applying feedback control techniques to actively detumble or despin the debris after it has been captured. Adaptive backstepping control has been shown to be successful at detumbling debris, albeit with the assumption of an inelastic tether [9]. A tether with a reel mechanism that can change the length of the tether was investigated as a way to despin a debris in a planar simulation [10]. A modified yo-yo mechanism was presented to detumble tethered debris with residual angular velocity along the tether axis [11].

All the works discussed thus far have considered a single tether joining the chaser to the target, as depicted in Fig. 1a. The main drawback of employing a single tether is it does not naturally dampen the attitude motion of the target very quickly. For this reason, some research was conducted on two-tether systems. The first appeared to be from Misra and Diamond [12], where two spacecraft were connected via two tethers, as shown in Fig. 1b. Numerical simulations indeed showed improvements in rotational behavior as compared to a single-tether configuration. More recently, a planar two-tether configuration, with a tether reel on each tether, was applied to the space debris problem by Qi et al. [13]. Simulations showed that this technique is effective at despinning debris.

Inspired by the despinning efficiency of the two-tether approach that, thus far, has been purely theoretical and has relied on tether-reel mechanisms, this Note presents and experimentally validates a new tether configuration. This configuration, named the subtether configuration, is shown in Fig. 1c; it falls between the single- and two-tether approaches. Specifically, it aims to passively increase the despinning ability of the TSS as compared to the single-tether configuration while decreasing the total tether mass required as compared to the two-tether configuration. Although not investigated in this Note, the reduction in tether use may decrease the risk of the tethers becoming entangled relative to the two-tether configuration. This subtether configuration was previously employed by the authors to detumble debris in onorbit simulations [14], and it is simplified to its planar form in this Note to allow for experimental validation. The tether leaving the chaser is denoted the main tether, and the two tethers connecting the main tether to the target are denoted as subtethers. The point where the main tether splits into subtethers is named the junction. The approach taken herein is to use the viscoelastic properties of the main tether and subtethers to regulate the relative angular motion of the uncooperative target, i.e., to despin the debris. It should be noted that neither feedback control nor tether reels are used to despin the debris; instead, the tether material damping is used to passively despin the debris, which is an effect that is enhanced by the proposed tether configuration as compared to the single-tether configuration. Unlike existing TSS despinning

Presented as Paper 2017-1049 at the AIAA Guidance, Navigation, and Control Conference, Grapevine, TX, 9–13 January 2017; received 10 May 2017; revision received 14 July 2017; accepted for publication 31 July 2017; published online 18 September 2017. Copyright © 2017 by Kirk Hovell and Steve Ulrich. Published by the American Institute of Aeronautics and Astronautics, Inc., with permission. All requests for copying and permission to reprint should be submitted to CCC at [www.copyright.com](http://www.copyright.com); employ the ISSN 0731-5090 (print) or 1533-3884 (online) to initiate your request. See also AIAA Rights and Permissions [www.aiaa.org/randp](http://www.aiaa.org/randp).

\*Graduate Student, Department of Mechanical and Aerospace Engineering, 1125 Colonel By Drive, Student Member AIAA.

<sup>†</sup>Assistant Professor, Department of Mechanical and Aerospace Engineering, 1125 Colonel By Drive, Senior Member AIAA.

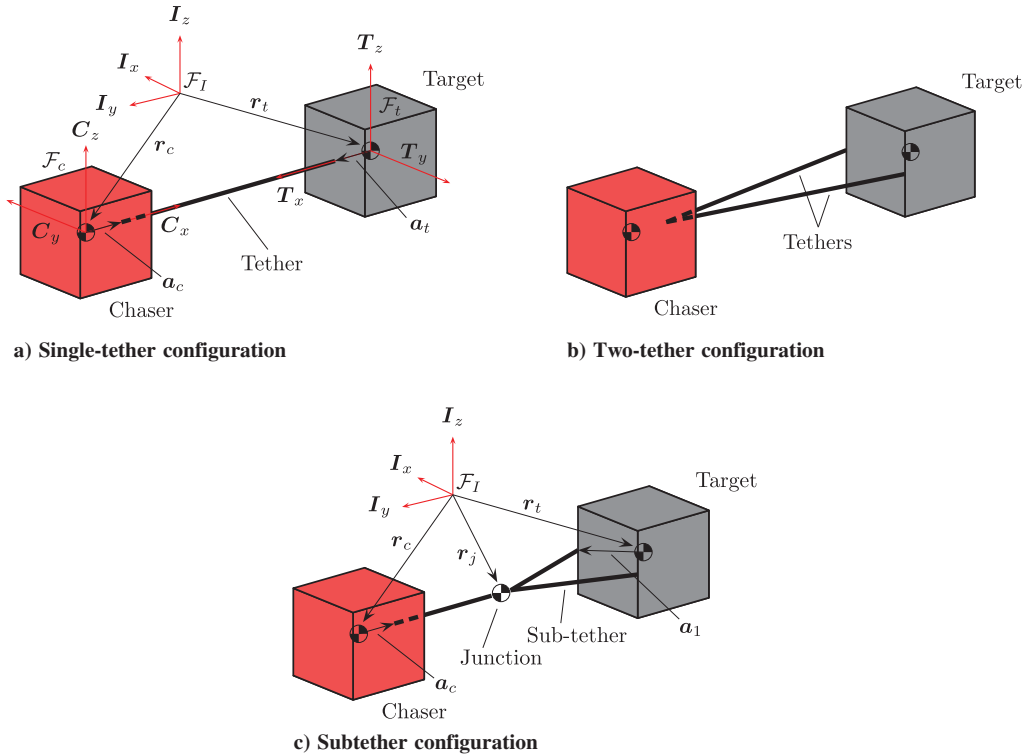


Fig. 1 Showcase of tether configurations.

approaches, this work bridges the gap between theory and practice by experimentally demonstrating the stabilization of spinning debris using tethers. In addition, in contrast with previous works that modeled tethers in simulations as either an inelastic material [6,9], an elastic material without damping [7,12], or an elastic material with constant stiffness and damping [3–5,8,10,13,14], a new nonlinear tether stiffness model is herein proposed. This new formulation models the tether stiffness as a nonlinear function of its stretch; as such, it better captures the experimental tether physical characteristics. In view of the aforementioned, the original contributions of this Note to the field of tethered space debris despinning are 1) the introduction of a new subtether configuration; 2) the inclusion of a nonlinear tether stiffness model; and 3) the first, to our knowledge, experiments demonstrating the despinning of debris using tethers.

This Note is organized as follows: Sec. II presents the equations of motion for the single tether and the new, proposed, subtether TSS configurations in a planar laboratory-representative environment. Then, in Sec. III, numerical simulations are performed to compare the despinning performance of both tether configurations. Section IV discusses the planar experimental setup, presents experimental results, and compares those results to the simulated results for both tether configurations. Finally, Sec. V draws conclusions on the work presented.

## II. Dynamics

Referring to Figs. 1a and 1c,  $\mathcal{F}_t$  and  $\mathcal{F}_c$  represent body-fixed reference frames attached to the target and chaser, respectively; and  $\mathcal{F}_I$  represents an inertially fixed reference frame. The position of the center of mass of the target, chaser, and junction are described by position vectors  $r_t$ ,  $r_c$ , and  $r_j$ , respectively, in  $\mathcal{F}_I$ . The target and chaser are modeled as rigid bodies, and the junction is modeled as a point mass. Each tether is modeled as a massless spring-damper system with a nonlinear stiffness, as shown in Fig. 2.

A Newton–Euler approach is taken to model the planar dynamics of the single-tether and subtether TSS configurations.

### A. Single-Tether Dynamics

The planar single-tether equations that describe the motion of the system shown in Fig. 1a are as follows:

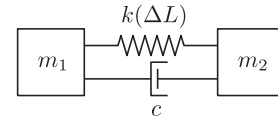


Fig. 2 Nonlinear viscoelastic tether model.

$$\ddot{\mathbf{r}}_t = \frac{\mathbf{F}_s}{m_t} \quad (1)$$

$$\ddot{\mathbf{r}}_c = -\frac{\mathbf{F}_s}{m_c} \quad (2)$$

$$\ddot{\theta}_t = \frac{1}{J_{zz,t}} \mathbf{a}_t^x(\mathbf{A}(\theta_t) \mathbf{F}_s) \quad (3)$$

$$\ddot{\theta}_c = -\frac{1}{J_{zz,c}} \mathbf{a}_c^x(\mathbf{A}(\theta_c) \mathbf{F}_s) \quad (4)$$

where  $m_t$ ,  $m_c$ ,  $J_{zz,t}$ , and  $J_{zz,c}$  are the masses and moment of inertias of the target and chaser, respectively. The single-tether attachment point to the target and chaser, in their respective body-fixed reference frames and with respect to their center of masses, are given by  $\mathbf{a}_t$  and  $\mathbf{a}_c$ . The attitudes of the target and chaser are given by  $\theta_t$  and  $\theta_c$ , respectively, and represent rotations about the  $I_z$  axis. The attitude matrix  $\mathbf{A}(\theta)$  describes a rotation from the inertial reference frame  $\mathcal{F}_I$  to the body-fixed frame corresponding to  $\theta$  through the following:

$$\mathbf{A}(\theta) = \begin{bmatrix} \cos(\theta) & \sin(\theta) & 0 \\ -\sin(\theta) & \cos(\theta) & 0 \\ 0 & 0 & 1 \end{bmatrix} \quad (5)$$

Finally,  $\mathbf{F}_s$  is the single-tether tension. Although many other researchers [3–5,8,10,13,14] used a constant-stiffness-based tether model of the following form:

$$\mathbf{F}_s = \begin{cases} \left[ k_s \Delta L_s + c_s \dot{\mathbf{L}}_s^T \frac{\mathbf{L}_s}{\|\mathbf{L}_s\|} \right] \frac{\mathbf{L}_s}{\|\mathbf{L}_s\|}, & \text{for } \Delta L_s > 0 \\ \mathbf{0}, & \text{otherwise} \end{cases} \quad (6)$$

a nonlinear stretched-based tether stiffness model is herein proposed. As will be shown in Sec. IV, this model better captures the nonlinear behavior inherent to elastic tethers. This model is given by the following:

$$\mathbf{F}_s = \begin{cases} \left[ k_s(\Delta L_s) \Delta L_s + c_s \dot{\mathbf{L}}_s^T \frac{\mathbf{L}_s}{\|\mathbf{L}_s\|} \right] \frac{\mathbf{L}_s}{\|\mathbf{L}_s\|}, & \text{for } \Delta L_s > 0 \\ \mathbf{0} & \text{otherwise} \end{cases} \quad (7)$$

where  $k_s(\Delta L_s)$  is the nonlinear stiffness as a function of the stretch  $\Delta L_s$ ;  $c_s$  is the single-tether damping; and  $\mathbf{L}_s$  represents the single-tether vector components in  $\mathcal{F}_I$ , given by the following:

$$\mathbf{L}_s = \mathbf{r}_c + \mathbf{A}(\theta_c)^T \mathbf{a}_c - \mathbf{r}_t - \mathbf{A}(\theta_t)^T \mathbf{a}_t \quad (8)$$

The single-tether stretch  $\Delta L_s$  is

$$\Delta L_s = \|\mathbf{L}_s\| - L_{0,s} \quad (9)$$

where  $L_{0,s}$  is the nominal length of the single tether. The tether derivative  $\dot{\mathbf{L}}_s$  is given by the following:

$$\dot{\mathbf{L}}_s = \dot{\mathbf{r}}_c + \mathbf{A}(\theta_c)^T \boldsymbol{\omega}_c^\times \mathbf{a}_c - \dot{\mathbf{r}}_t - \mathbf{A}(\theta_t)^T \boldsymbol{\omega}_t^\times \mathbf{a}_t \quad (10)$$

where  $\boldsymbol{\omega}$ , and  $\boldsymbol{\omega}_c$  are the angular rate vector components of the target and chaser, respectively. For this planar analysis,  $\boldsymbol{\omega}$  is constrained to have the following form:

$$\boldsymbol{\omega} = \begin{bmatrix} 0 \\ 0 \\ \dot{\theta} \end{bmatrix} \quad (11)$$

## B. Subtether Dynamics

The planar subtether equations that describe the motion of the TSS shown in Fig. 1c are

$$\ddot{\mathbf{r}}_i = \sum_{i=1}^2 \frac{\mathbf{F}_i}{m_i} \quad (12)$$

$$\ddot{\mathbf{r}}_c = -\frac{\mathbf{F}_m}{m_c} \quad (13)$$

$$\ddot{\mathbf{r}}_j = \frac{\mathbf{F}_m}{m_j} - \sum_{i=1}^2 \frac{\mathbf{F}_i}{m_j} \quad (14)$$

$$\ddot{\theta}_t = \frac{1}{J_{zz,t}} \sum_{i=1}^2 \mathbf{a}_i^\times(\mathbf{A}(\theta_t) \mathbf{F}_i) \quad (15)$$

$$\ddot{\theta}_c = -\frac{1}{J_{zz,c}} \mathbf{a}_c^\times(\mathbf{A}(\theta_c) \mathbf{F}_m) \quad (16)$$

where  $m_j$  is the mass of the junction,  $\mathbf{F}_i \forall i = 1, 2$  is the tension in the two subtethers, and  $\mathbf{F}_m$  is the tension in the main tether, given by the following:

$$\mathbf{F}_i = \begin{cases} \left[ k(\Delta L_i) \Delta L_i + c \dot{\mathbf{L}}_i^T \frac{\mathbf{L}_i}{\|\mathbf{L}_i\|} \right] \frac{\mathbf{L}_i}{\|\mathbf{L}_i\|}, & \text{for } \Delta L_i > 0; \quad \forall i = 1, 2 \\ \mathbf{0}, & \text{otherwise} \end{cases} \quad (17)$$

$$\mathbf{F}_m = \begin{cases} \left[ k(\Delta L_m) \Delta L_m + c \dot{\mathbf{L}}_m^T \frac{\mathbf{L}_m}{\|\mathbf{L}_m\|} \right] \frac{\mathbf{L}_m}{\|\mathbf{L}_m\|}, & \text{for } \Delta L_m > 0 \\ \mathbf{0}, & \text{otherwise} \end{cases} \quad (18)$$

where the stiffness  $k(\Delta L)$  is a nonlinear function of the stretch,  $\Delta L_i$  or  $\Delta L_m$ , in the  $i$ th subtether or main tether, respectively. The damping constant of the subtethers and main tether is represented by  $c$ . The tether vector components in  $\mathcal{F}_I$  are represented by  $\mathbf{L}_i$  for each subtether and  $\mathbf{L}_m$  for the main tether, and they are obtained through the following:

$$\mathbf{L}_i = \mathbf{r}_j - \mathbf{r}_t - \mathbf{A}(\theta_t)^T \mathbf{a}_i, \quad \forall i = 1, 2 \quad (19)$$

$$\mathbf{L}_m = \mathbf{r}_c + \mathbf{A}(\theta_c)^T \mathbf{a}_c - \mathbf{r}_j \quad (20)$$

The stretches in the tethers are calculated as follows:

$$\Delta L_i = \|\mathbf{L}_i\| - L_{0,i}, \quad \forall i = 1, 2 \quad (21)$$

$$\Delta L_m = \|\mathbf{L}_m\| - L_{0,m} \quad (22)$$

where  $L_{0,i} \forall i = 1, 2$ , and  $L_{0,m}$  are the unstretched lengths of the subtethers and main tether, respectively. The tether derivatives are as follows:

$$\dot{\mathbf{L}}_i = \dot{\mathbf{r}}_j - \dot{\mathbf{r}}_t - \mathbf{A}(\theta_t)^T \boldsymbol{\omega}_t^\times \mathbf{a}_i, \quad \forall i = 1, 2 \quad (23)$$

$$\dot{\mathbf{L}}_m = \dot{\mathbf{r}}_c + \mathbf{A}(\theta_c)^T \boldsymbol{\omega}_c^\times \mathbf{a}_c - \dot{\mathbf{r}}_j \quad (24)$$

To simulate the motion, Eqs. (1–4) and (12–16) are numerically integrated.

## III. Numerical Simulation

This section presents numerical simulations that compare the effect of tether configuration on the TSS's ability to despin debris. These planar simulations will be experimentally validated in Sec. IV. To quantify the performance of the despinning process, the target tether angle and angular rate are shown. The tether angle is a measurement of the attitude of the target with respect to the tether, depicted in Fig. 3. It is calculated as follows:

$$\phi = \cos^{-1} \left( \left( \mathbf{A}(\theta_t)^T \mathbf{T}_x \right)^T \frac{\mathbf{L}_s}{\|\mathbf{L}_s\|} \right) \quad (25)$$

where  $\mathbf{T}_x$  are the components of the unit vector in the  $x$  direction in  $\mathcal{F}_I$ . The proposed subtether configuration uses a hypothetical single tether to calculate the tether angle, such that both tether configurations can be readily compared.

The tether stiffness is modeled to be a nonlinear function of its stretch, according to Fig. 4. This stiffness model was experimentally determined from the tethers that are used in experimentation. A spline was fit through the data to determine the tether stiffness for a given stretch. The damping constants were experimentally determined by performing an independent simulation and experiment using the facility described in Sec. IV.A. Because damping primarily affects the decay rate of the vibration, the damping parameter in the simulation was adjusted until similar decay rates between the simulation and

experiment were observed. Then, the damping values were held constant for all subsequent simulations.

Maintaining tension in the tethers allows the tether damping to reduce the angular motion of the spinning target, and it ensures that a collision between the chaser and the target is avoided. A TSS barycenter spin approach to despin a debris is herein presented. That is, the chaser and target spin about the TSS barycenter, such that the centripetal force maintains tension in the tethers while the tethers despin the target with respect to the chaser. This represents a technique for despining debris that does not require fuel, other than that required to initiate the barycenter spin. Simulation parameters and initial conditions are listed in Tables 1 and 2, respectively. The simulation is performed over 30 s with a discrete trapezoidal integrator in MATLAB/Simulink using a 0.002 second fixed time step.

The TSS is initially spinning about its barycenter, and then the target is given an angular rate of  $\theta_t = 79$  deg/s at  $t = 2$  s to simulate a spinning target being captured while the TSS is spinning about its barycenter. Plots of the resulting motion are shown in Fig. 5. Figure 5a shows that, all else being equal, the subtether configuration maintains a lower target tether angle. Similarly, Fig. 5b shows that the initial angular rate of the target is dampened faster for the subtether configuration. As expected, the angular rate does not tend toward zero but converges to the spin rate of the TSS about its barycenter. The subtether configuration, through having tether attachment points on the extremities of the target, better exploits the material damping in the tethers. Note that the subtether configuration also demonstrates higher oscillation frequencies of the target, as is evident in Fig. 5b, which may induce longitudinal oscillations in the tether.

#### IV. Experimental Validation

To validate the numerical simulations, experiments are performed in a laboratory environment at Carleton University. A planar gravity-offset testbed is used, where two spacecraft platforms are tethered together on a

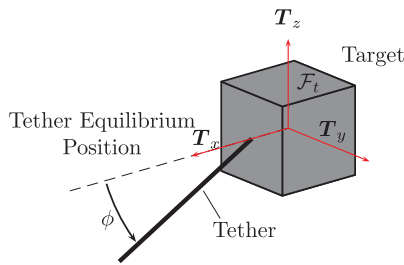


Fig. 3 Angle  $\phi$  representing the angle between the tether and  $T_x$ .

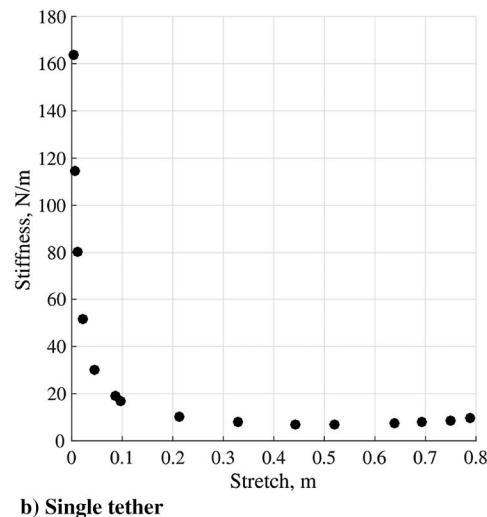
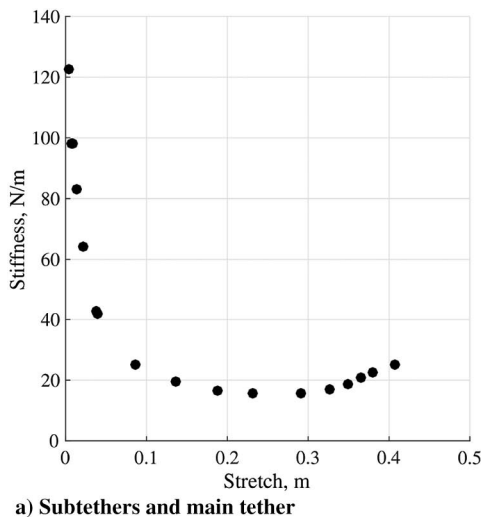


Fig. 4 Experimental nonlinear tether stiffness models.

Table 1 Parameters for simulations and experiments

Parameter	Value
$J_{zz,t}$ , $\text{kg} \cdot \text{m}^2$	0.22
$J_{zz,c}$ , $\text{kg} \cdot \text{m}^2$	0.30
$m_t$ , kg	12.19
$m_c$ , kg	17.24
$m_j$ , kg	0.01
$L_{0,m}$ , m	0.28
$L_{0,1}$ , m	0.28
$L_{0,2}$ , m	0.28
$L_{0,s}$ , m	0.54
$c_s$ , (N · s)/m	3.0
$c$ , (N · s)/m	1.1
$a_c$ , m	$[0.135, -0.009, 0]^T$
$a_1$ , m	$[0.110, 0.127, 0]^T$
$a_2$ , m	$[0.113, -0.094, 0]^T$
$a_t$ , m	$[0.110, 0.016, 0]^T$

Table 2 Initial conditions for simulations and experiments

Parameter	Value
$r_t$ , m	$[2.02, 0.74, 0]^T$
$r_c$ , m	$[2.80, 0.75, 0]^T$
$\theta_t$ , deg	0
$\theta_c$ , deg	180
$\dot{r}_t$ , m/s	$[0, -0.3, 0]^T$
$\dot{r}_c$ , m/s	$[0, 0.2, 0]^T$
$\dot{\theta}_t$ , deg/s	79

flat granite surface. Air bearings are used to provide a near-friction-free planar environment. The experimental facility is discussed, followed by the experimental setup and results.

#### A. Experiment Facility

Experiments were conducted at Carleton University's Spacecraft Robotics and Control Laboratory, using the spacecraft proximity operations testbed (SPOT). Specifically, the SPOT consists of two air-bearing spacecraft platforms operating in close proximity on a  $2.4 \times 3.7$  m granite surface. The use of air bearings on the platforms reduces the friction to a negligible level. Due to surface slope angles of 0.0026 and 0.0031 deg along both directions, residual gravitational accelerations of 0.439 and 0.525  $\text{mm/s}^2$  perturb the dynamics of the

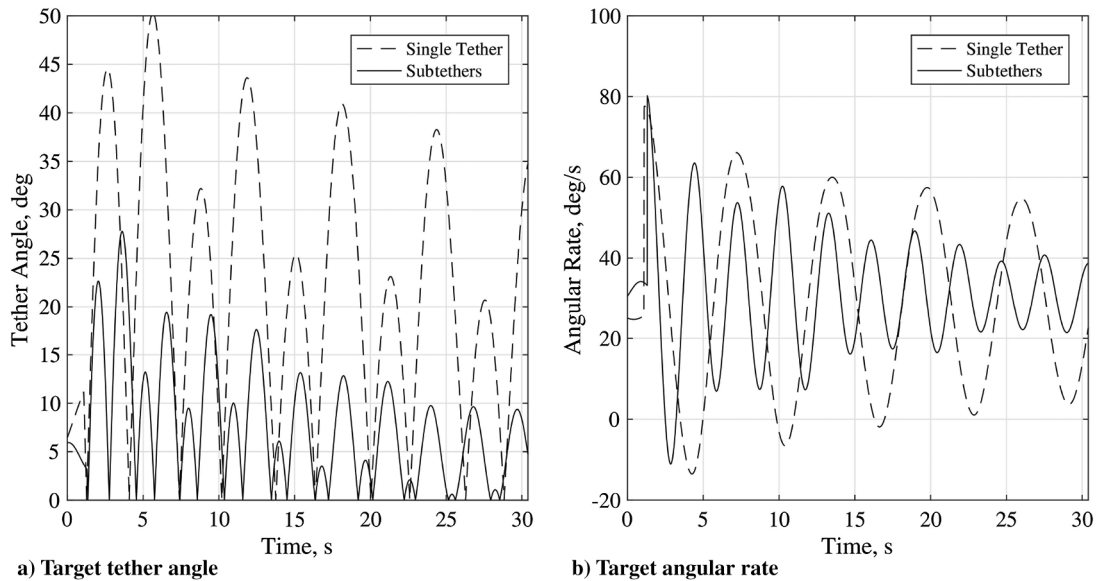


Fig. 5 Comparing the effect of tether configuration on target attitude motion.

floating platforms along the  $I_x$  and  $I_y$  directions, respectively. Both platforms have dimensions of  $0.3 \times 0.3 \times 0.3$  m and are actuated by expelling compressed air at 550 kPa through eight miniature air nozzles distributed around each platform, thereby providing full planar control authority. Each thruster generates approximately 0.25 N of thrust and is controlled at a frequency of 500 Hz by a pulsewidth modulation scheme using solenoid valves. Pressurized air for the thrusters and the air-bearing flotation system is stored on board in a single air cylinder at 31 MPa. The structure consists of an aluminum frame with four corner rods, on which three modular decks are stacked. To protect the internal components, the structure is covered with semitransparent acrylic panels. Figure 6 shows a fully assembled SPOT spacecraft platform.

The motion of both platforms is measured in real time through four active light-emitting diodes (LEDs) on each platform, which are tracked by an eight-camera PhaseSpace© motion-capture system. This provides highly accurate ground-truth position and attitude data. All motion-capture cameras are connected to a PhaseSpace server, which is connected to a ground station computer. The ground station computer communicates, via a wireless user datagram protocol, the ground-truth information to the platforms' onboard computers, which consist of Raspberry Pi-3s running the Raspbian Linux operating system. Based on the position and attitude data that the



Fig. 6 SPOT platform built at Carleton University.

platforms wirelessly receive, they can perform feedback control by calculating the required thrust to autonomously maneuver, as well as actuating the appropriate solenoid valves to realize this motion. The ground station computer also receives real-time telemetry data (i.e., any signals of interest, as specified by the user) from all onboard computers for post-experiment analysis purposes.

A MATLAB/Simulink numerical simulator that recreates the dynamics and emulates the different onboard sensors and actuators is first used to design and test the upcoming experiment. Once the performance in simulations is satisfactory, the control software is converted into C/C++ using Embedded Coder®, compiled, and then executed on the platforms' Raspberry Pi-3 computers.

## B. Experimental Setup

The simulation presented in Sec. III was chosen such that it is replicable experimentally. Experiment properties and initial conditions are the same as in Tables 1 and 2. The experiment consists of two SPOT platforms placed on the granite table and tethered together in both tether configurations presented. The tethers used are composed of 56% polyester and 44% rubber. The main tether and subtethers are 28 cm long each, and the single tether is 54 cm long to create equal separation between the two platforms regardless of tether configuration. Figure 7 shows both platforms in the subtether configuration. The black and red platforms represent the target and the chaser, respectively.

The platforms remain in contact with the table until a strong lock has been acquired on the LEDs by the motion-capture system. Following this, the platforms begin to float and move to the desired

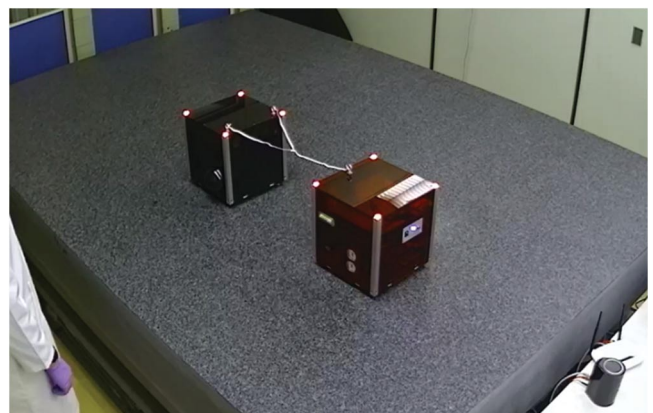


Fig. 7 Two experimental platforms in the subtether configuration.

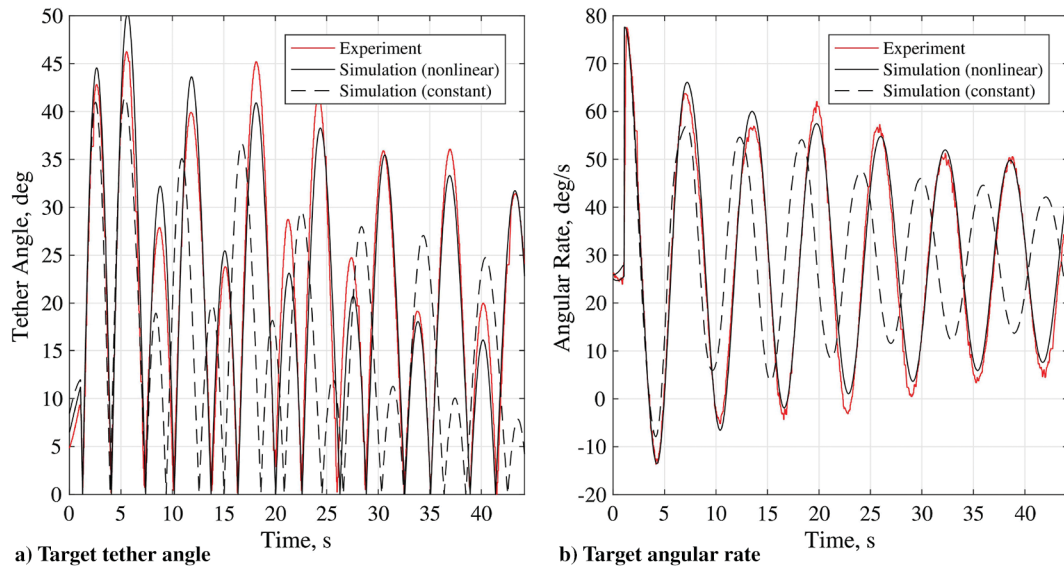


Fig. 8 Comparison of single-tether experimental and simulated results.

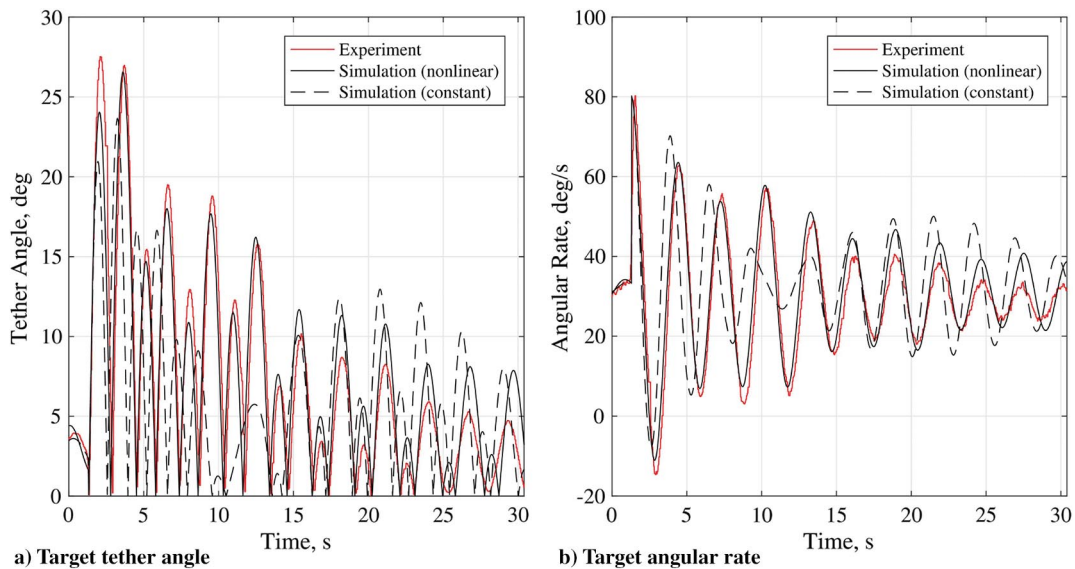


Fig. 9 Comparison of subtether experimental and simulated results.

initial conditions. Once the TSS barycenter spin has been initiated, the target is given an additional spinning motion. This creates the initial conditions of capturing a spinning debris while the TSS itself is rotating. Next, the target becomes fully passive, and the chaser uses its thrusters solely to maintain its  $C_x$  axis pointing at the target. The system coasts for 35 s, drifting due to the slight slope in the table, during which the damping in the tethers and subtethers reduces the relative angular motion of the target.

### C. Experimental Results

Supplemental video S1 shows a video of the single-tether experiment<sup>‡</sup>. Results from the single-tether experiments are compared to the single-tether simulated results in Fig. 8. To demonstrate the necessity of using a nonlinear-stiffness model to accurately capture the physical behavior of elastic tethers, simulation results that employ the constant stiffness model given in Eq. (6) are also shown. In an attempt to make an unbiased comparison between the constant-stiffness and the nonlinear-stiffness results, the constant tether stiffness value was chosen by using the average tether stretch

over the course of the simulation with Fig. 4 to determine the corresponding average stiffness. For the single tether, this average stiffness was found to be 18.5 N/m, and for the main tether and subtethers, it was found to be 53.3 N/m.

The tether angle is shown in Fig. 8a. The similarities between the nonlinear-stiffness simulated and experimental results are obvious, with only small discrepancies in the amplitude of the oscillations. These discrepancies may be attributed to numerous sources, including uncertainties in mass properties of the platforms, nonlinear tether damping, or unmodeled effects such as drag or friction between the air bearings and the granite table. The constant-stiffness tether model results in inaccurate predictions of the motion. The plot of the angular rate over time, shown in Fig. 8b, also has excellent correlation when the nonlinear-stiffness tether model is used, whereas the constant-stiffness tether leads to differences in amplitude and frequency of the motion. Indeed, the nonlinear model better represents the tether used in experiments.

Supplemental video S2 shows a video of the subtether experiment,<sup>§</sup> and experimental results are compared to simulated results in Fig. 9. The experiment and nonlinear-stiffness simulation are well correlated once again, as shown in Fig. 9a, where only minor tether angle

<sup>‡</sup>Video available online at <https://goo.gl/NpmazF> [retrieved 2017].

<sup>§</sup>Video available online at <https://goo.gl/iLbDdH> [retrieved 2017].

discrepancies are observed. The target angular rate, shown in Fig. 9b, shows superior correlation between the simulated and experimental results when the nonlinear-stiffness tether model is used. The steady-state angular rate is slightly lower in the experiment as compared to the simulation, which is likely due to drag and friction slowing the TSS barycenter spin over time. The low errors between the simulated and experimental results validate the equations of motion and nonlinear-stiffness tether model presented in this Note.

## V. Conclusions

Two tethered spacecraft system (TSS) configurations were presented: one with a single tether joining the two spacecraft, and a new one with subtethers that were attached to the target at various locations. This Note provided the equations of motion for both TSS configurations in a planar environment. Planar simulations, which included an experimentally obtained nonlinear tether stiffness model, were performed that demonstrated the improved despinning abilities of the subtether configuration as compared to the single-tether configuration. Planar experimental results were compared with the simulation results and successfully validated the developed equations of motion and the tether model presented. The proposed subtether configuration better exploits tether damping and leads to improved despinning performance as compared to the single-tether configuration. The experiments are the first, to the authors' knowledge, that demonstrate the despinning of a debris using tethers.

## Acknowledgments

This research was financially supported in part by the Natural Sciences and Engineering Research Council of Canada under the Canada Graduate Scholarship CGS M-302098-2015, the Discovery Grant program, and the Ontario Graduate Scholarship.

## References

- [1] Kessler, D. J., and Cour-Palais, B. G., "Collision Frequency of Artificial Satellites: The Creation of a Debris Belt," *Journal of Geophysical Research*, Vol. 83, No. A6, 1978, pp. 2637–2646. doi:10.1029/JA083iA06p02637
- [2] Wormnes, K., Le Letty, R., Summerer, L., Schonenborg, R., Dubois-Matra, O., Luraschi, E., Cropp, A., Krag, H., and Delaval, J., "ESA Technologies for Space Debris Remediation," *6th European Conference on Space Debris*, ESA Communications, ESTEC, Noordwijk, The Netherlands, 2013, pp. 1–8.
- [3] Aslanov, V. S., and Yudinsev, V. V., "Dynamics of Large Debris Connected to Space Tug by a Tether," *Journal of Guidance, Control, and Dynamics*, Vol. 36, No. 6, 2013, pp. 1654–1660. doi:10.2514/1.60976
- [4] Aslanov, V. S., and Yudinsev, V. V., "Dynamics of Large Space Debris Removal Using Tethered Space Tug," *Acta Astronautica*, Vol. 91, Oct.–Nov. 2013, pp. 149–156. doi:10.1016/j.actaastro.2013.05.020
- [5] Aslanov, V. S., and Yudinsev, V. V., "Behavior of Tethered Debris with Flexible Appendages," *Acta Astronautica*, Vol. 104, No. 1, 2014, pp. 91–98. doi:10.1016/j.actaastro.2014.07.028
- [6] Aslanov, V. S., and Yudinsev, V. V., "The Motion of Tethered Tug-Debris System with Fuel Residuals," *Advances in Space Research*, Vol. 56, No. 7, 2015, pp. 1493–1501. doi:10.1016/j.asr.2015.06.032
- [7] Aslanov, V. S., and Ledkov, A. S., "Dynamics of Towed Large Space Debris Taking into Account Atmospheric Disturbance," *Acta Mechanica*, Vol. 225, No. 9, 2014, pp. 2685–2697. doi:10.1007/s00707-014-1094-4
- [8] Mantellato, R., Lorenzini, E. C., Sternberg, D., Roascio, D., Saenz-Otero, A., and Zachrau, H., "Simulation of a Tethered Microgravity Robot Pair and Validation on a Planar Air Bearing," *Acta Astronautica*, Vol. 138, Sept. 2017, pp. 579–589. doi:10.1016/j.actaastro.2016.12.029
- [9] Huang, P., Wang, D., Meng, Z., Zhang, F., and Guo, J., "Adaptive Postcapture Backstepping Control for Tumbling Tethered Space Robot-Target Combination," *Journal of Guidance, Control, and Dynamics*, Vol. 39, No. 1, 2016, pp. 150–156. doi:10.2514/1.G001309
- [10] Meng, Z., Wang, B., and Huang, P., "Twist Suppression Method of Tethered Towing for Spinning Space Debris," *Journal of Aerospace Engineering*, Vol. 30, No. 4, 2017, Paper 04017012. doi:10.1061/(ASCE)AS.1943-5525.0000708
- [11] Yudinsev, V., and Aslanov, V., "Detumbling Space Debris Using Modified Yo-Yo Mechanism," *Journal of Guidance, Control, and Dynamics*, Vol. 40, No. 3, 2017, pp. 714–721. doi:10.2514/1.G000686
- [12] Misra, A. K., and Diamond, G. S., "Dynamics of a Subsatellite System Supported by Two Tethers," *Journal of Guidance, Control, and Dynamics*, Vol. 9, No. 1, 1986, pp. 12–16. doi:10.2514/3.20059
- [13] Qi, R., Misra, A. K., and Zuo, Z., "Active Debris Removal Using Double-Tethered Space-Tug System," *Journal of Guidance, Control, and Dynamics*, Vol. 40, No. 3, 2017, pp. 722–730. doi:10.2514/1.G000699
- [14] Hovell, K., and Ulrich, S., "Attitude Stabilization of an Uncooperative Spacecraft in an Orbital Environment Using Visco-Elastic Tethers," *AIAA Guidance, Navigation, and Control Conference*, AIAA Paper 2016-0641, 2016.